Article

Enhancement of Optical Adaptive Sensing by Using a Dual-Stage Seesaw-Swivel Actuator with a Tunable Vibration Absorber

Po-Chien Chou †, Yu-Cheng Lin † and Stone Cheng *

Department of Mechanical Engineering, National Chiao Tung University, No. 1001, University Road, Hsinchu 30010, Taiwan; E-Mails: arthurking8@msn.com (P.-C.C.); owan0518@hotmail.com (Y.-C.L.)

* Author to whom correspondence should be addressed; E-Mail: stonecheng@mail.nctu.edu.tw; Tel.: +886-3-571-2121 ext. 55204; Fax: +886-3-572-0634.

† These authors contributed equally to this work.

Abstract: Technological obstacles to the use of rotary-type swing arm actuators to actuate optical pickup modules in small-form-factor (SFF) disk drives stem from a hinge's skewed actuation, subsequently inducing off-axis aberrations and deteriorating optical quality. This work describes a dual-stage seesaw-swivel actuator for optical pickup actuation. A triple-layered bimorph bender made of piezoelectric materials (PZTs) is connected to the suspension of the pickup head, while the tunable vibration absorber (TVA) unit is mounted on the seesaw swing arm to offer a balanced force to reduce vibrations in a focusing direction. Both PZT and TVA are designed to satisfy stable focusing operation operational requirements and compensate for the tilt angle or deformation of a disc. Finally, simulation results verify the performance of the dual-stage seesaw-swivel actuator, along with experimental procedures and parametric design optimization confirming the effectiveness of the proposed system.

Nomenclature

|			
L_{PZT}	Effective length of PZT (mm)	d_{31}	Charging constant of PZT (C/N)
L_{arm}	Effective Length of arm (mm)	V_{PZT}	PZT input Voltage (V)
D_{disc}	Distance from disk center(mm)	A	The frequency ratio between system and input
ϕ	Rotary angle of PZT bender (rad)	B	The frequency ratio between system and TVA
θ	Rotary angle of arm (rad)	M	Mass ratio between system and TVA
γ	Rotary angle of disk (rad)	m_{sys}	Mass of dual-stage system (kg)
b	Width of PZT bender (mm)	m_{abs}	Mass of TVA (kg)
t_{PZT}	Thickness of PZT (mm)	C_{PZT}	Damping constant of PZT
t_{carbon}	Thickness of carbon (mm)	C_{sys}	Damping constant of arm
ρ_{PZT}	Density of PZT (kg/m^3)	C_{abs}	Damping constant of TVA
ρ_{carbon}	Density of carbon (kg/m^3)	k_{sys}	Stiffness of system (N/m)
ρ_{abs}	Density of TVA (kg/m^3)	k_{PZT}	Stiffness of PZT (N-m/rad)
E_{PZT}	Young's modulus of PZT (GPa)	k_{eq}	Equivalent stiffness of PZT (N/m)
E_{carbon}	Young's modulus of carbon (GPa)	k_{abs}	Stiffness of TVA (N/m)
I_{PZT}	Moment of inertia, PZT (m^4)	ζ_{sys}	Damping ratio of dual-stage system
I_{carbon}	Moment of inertia, carbon (m^4)	ζ_{abs}	Damping ratio of TVA

1. Introduction

Swing arm actuators have been applied to small form factor (SFF) optical pickup heads or near field hybrid recording systems. Trends in optical disk drives include developing small-form-factor (SFF) for holographic optics and extending the applications of near-field optics. In such a high speed positioning servo system, the head/disk spacing variation must be maintained as small as possible during disk operations. While attempting to reduce the size of optical heads, several works have scaled down all components of a conventional unit [1,2] and simplified the optical configuration, and micro optical elements, such as lenses and prisms. Other approaches integrate an optical module with a seesaw swivel actuator [3,4].

Two possible actuated mechanisms are available for active and passive head-positioning control. For active actuation, Yeack-Scranton devised a secondary stage PZT bender with an active slider for contact recording [5]. Following the PZT actuator and its applications, Tagawa proposed a self-loading slider featuring a twin structure piezo-actuator to maintain constant flying height spacing [6]. Kajitani developed an active slider associated with multilayered piezo-actuators to compensate for flying height variation [7]. In contrast with the above track-seek operations, Jun and Takashi investigated the feasibility of using a circular arc slider driven by a piezoelectric actuator to reduce the tilt motions of the lens in pitching/rolling directions [8]. Liu investigated the feasibility of a dynamic motion approach for a piezotube actuator subjected to disk deformation [9]. Moreover, in study involving a multilayered structure, Woosung used a flexure hinge mechanism to extend the allowable stroke to tracking and focusing motions [10]. Additionally, passive mass absorber utilizes an inertial mass and tuned support to mitigate mechanical vibration. Chung introduced a two-dimensional vibration model of a feeding deck system to reduce in-plane vibration [11]. According to their functional and structural

identification, Heo characterized the dynamic behavior of a passive damper consisting of a rubber bobbin and plate ring [12]. Moreover, Chung established a design procedure to combine passive and active devices with an enlarged bandwidth control. That adaptive dynamic absorber is embedded with a voice coil motor (VCM) device [13]. However, to make use of the hollow space within the VCM, Jiang investigated the feasibility of a tuned dual mass damping device [14]. In particular, Kuwajima developed a novel shockproof structure by using a balanced type suspension, as well as investigated its performance on external shock resistance during read/write operations [15].

This work describes a novel a dual-stage seesaw-swivel actuator based on optical sensing by using a PZT bimorph component to compensate for the tilt angle variation in focusing stroke. A piezoelectric actuated suspension for a secondary-stage actuator is also developed to implement fine head positioning to assist the primary VCM actuator and maintain a constant flying height during the focusing operation, as shown in Figure 1. The secondary micro actuator functions mainly for fine and fast compensation, while a conventional VCM performs coarse positioning. A dynamic model for a bimorph structure is also developed to optimize and verify the natural frequency of actuating behavior. Additionally, a two dimensional vibration model of the optical sensing device with the absorber is established to ensure system stability and robustness. Based on multi-body dynamic analysis, a balanced mass associated with two cantilever springs provides a rotational reaction to the moving part under seesaw actuation. Moreover, this work investigates the feasibility of implementing a passive tunable vibration absorber (TVA) for spacing variation and head positioning control endowed with a bimorph micro actuator. Finally performance of biaxial motion is evaluated based on numerical simulations of optimization and experimental results.

Figure 1. Schematic illustration of the bimorph dual-stage actuator with the TVA unit indicated.
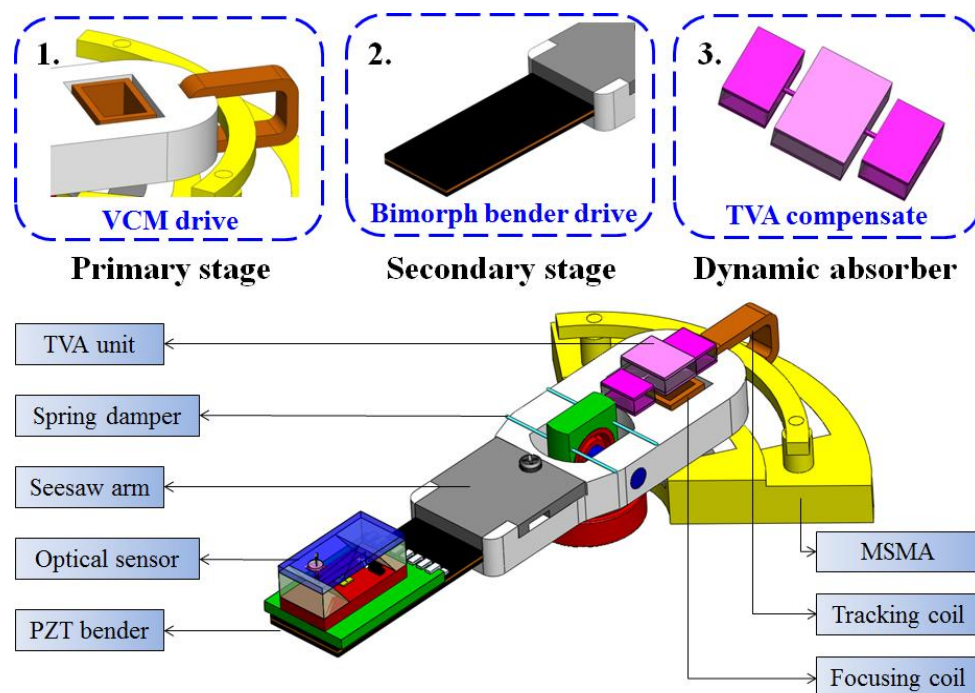
2. Mechanical Design and Theoretical Analysis

The optical axis shift during the primary VCM actuation is compensated for by using the active bimorph micro actuator. A TVA can passively absorb the residual tilt variations while actively generating a reacting force for the moment conservation. The proposed mechanism is a seesaw type swivel actuator using piezoelectric active control collaboratively with passive TVA design. The following sections describe the proposed mechanism.

2.1. Angular Deviation Compensation

In actuated slider suspension, the tilt motion of the optical actuator causes the variation of focal spot position on the photo-detector, as shown in Figure 2. The middle figure of light intensity distribution is a well-symmetric focal spot on the PD center without tilting angle. If the focusing motion is achieved by z seesaw-type arm which generates a ±0.1° nutating angle, the returning beam would not be orthogonal to the optical sensor. The reflected focal spot on the PD will shift away from the center and the light distributions will approach one side of the photo-diode. Hence, given the increasing accuracy of head positioning, a drive capable of tilt control is necessary to reduce the tilt margin as the optical aberration is correspondingly increased. A compensation scheme is also developed for optical axis in-line calibration, and evaluated by driving a simply bimorph PZT bender.

Figure 2. Misalignment in the incline angle of the optical axis.
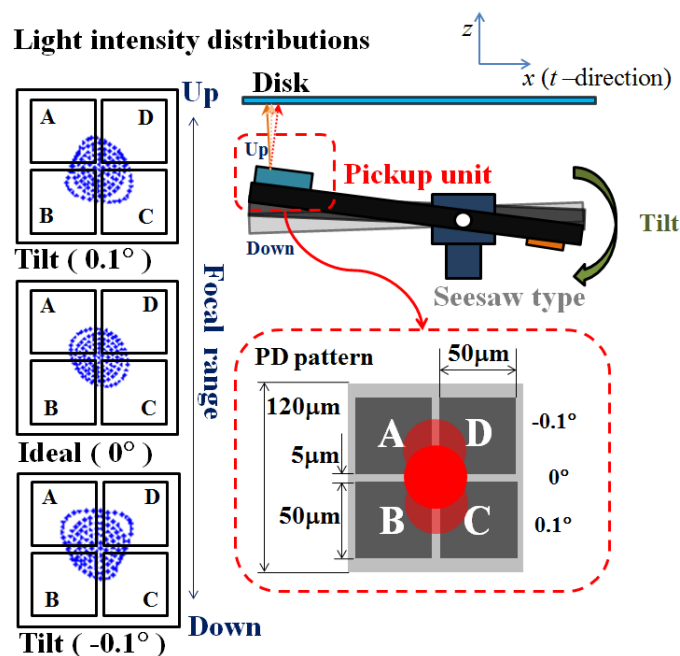

2.2. Dual-Stage Leveraged Mechanism

A common method of piezoelectric actuated suspension is driven along the opposite data (track) tangential direction in an allowable stroke. The proposed seesaw swivel-drive actuator uses a dual-stage leverage mechanism (Figure 3), through use of a coarse movement via VCM control and a secondary fine positioning via PZT. As PZT compensates the tilt angle of seesaw arm in the opposite

way—the laser beam will be kept in orthogonal to the disk (Figure 3, left). Hence, PZT tilt control fixes the tangential displacement of focusing, and calibrates the asymmetry of the S-curve. Complete two-axis scanning is then performed by independently controlling the dual stage actuators.

Figure 3. Conceptual diagram of the combined bimorph piezo-VCM actuator based active tilt compensation.
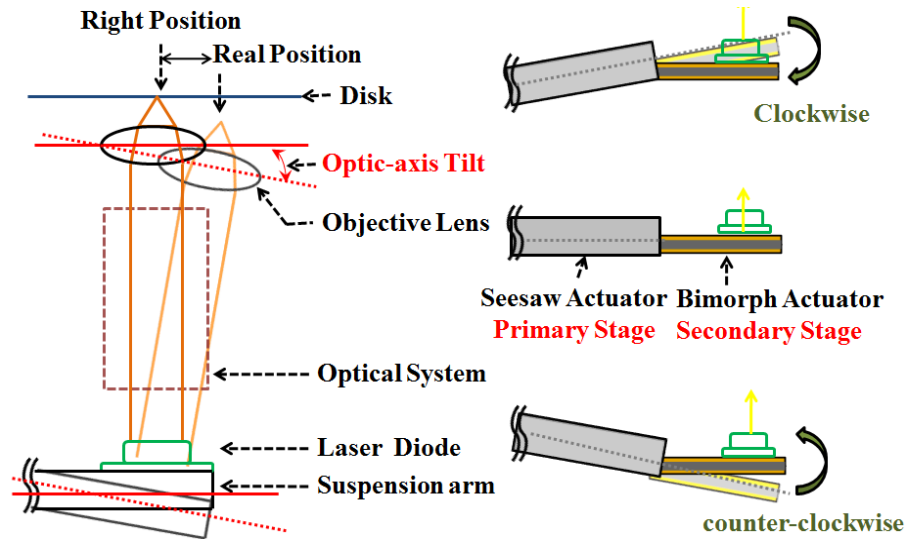
2.3. Cantilever TVA Structure

The primary structure with arbitrary distributions of mass, stiffness and damping is subjected to vibration suppression by an absorber subsystem. Sensing variation capabilities in the optic-axis direction are investigated to ensure the suppression of robust vibration. Consisting of two flexible cantilever beams extended from a balanced mass, a cantilever TVA subsystem is illustrated from the perspective of both improving bandwidth and increasing shock protection.

Figure 4. Developed tunable vibration absorber with system dynamics behavior: principles and practices.
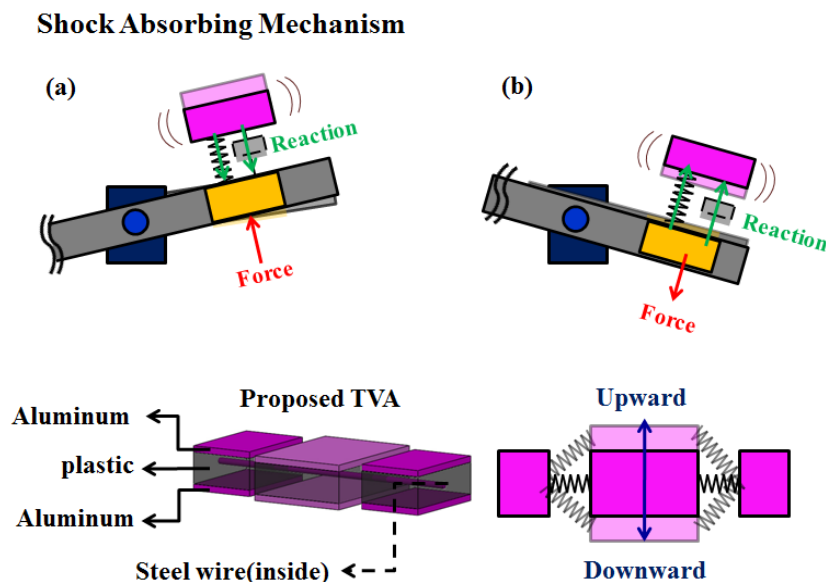
The vibration suppression of structures is based on independent design of dynamic absorbers, while taking into account the selected tuning mass of the subsystem structure. Effective structural stiffness is thus adjusted by adjusting the beam dimensions after a preliminary primitive design. Figure 4 illustrates the structural configuration of this work, which consists of a three-block structure called "soundmetal" that is pinned by a flexible wire.

3. Numerical Analysis

DeVoe and Pisano [16] developed a model for piezoelectric multi-morph cantilevers extended from Timoshenko's approach to investigate the deflection of micro-actuators. To derive a simple working equation, Weinberg [17] obtained a simple closed-form solution for the bending of piezoelectric multi-morphs by using the Euler-Bernoulli beam theory and integrated equilibrium equations. This theory assumes that cross sections remain plane and normal to the deformed beam axis. Such assumptions are appropriate given the slender geometry of typical multi-morphs. Krommer developed the constitutive equations of a multi-morph by assuming two-dimensional kinematics of the structure [18]. Ha and Kim attempted to optimize bimorphs in order to maximize the tip stroke or vertical displacement by using the thickness ratio between the substrate (or shim layer) and PZT layers [19]. Pursuing a high bandwidth and a sufficient optical performance of the combined piezo-VCM actuator and design parameters of the PZT bender (*i.e.*, length, width and thickness) are of priority concern. Generally, the rotary angle and deflection of the PZT bender is proportion to the square and cube of the length of the PZT bender (by basic beam theory). Other parameters affect the bandwidth (fundamental frequency).

3.1. Rotary Angle of PZT Bender

Figure 5 displays a "sandwich"-like PZT that consists of a carbon fiber chip with two d_{31}-type PZT ceramics. This figure also considers a small piece element in the upper PZT material, in which the corresponding extension can be evaluated as follows:

$$\frac{\Delta L_{PZT}}{L_{PZT}} = \frac{d_{31} V_{PZT}}{t_{PZT}}$$
(1)

The elongation force ΔF and momentum ΔM generated by the small element in the Figure 4(a) are:

$$\Delta M = \Delta F \cdot z = \frac{d_{31} V_{PZT} b E_{PZT}}{t_{PZT}} z dz$$
(2)

Therefore, integrating Equation (2), the sum of bending moment in Figure 4 generated by the bimorph piezoelectric material is as follows:

$$M = d_{31} \cdot V_{PZT} \cdot E_{PZT} \cdot b \cdot \left(t_{PZT} + t_{carbon}\right)$$
(3)

Figure 5(a) shows a composed triple-layer beam that consists of both carbon fiber and piezoelectric material. The flexural rigidity of a multilayered beam is:

$$E_{eq} I_{eq} = E_{PZT} I_{PZT} + E_{carbon} I_{carbon}$$
(4)

where k_{PZT} is considered the stiffness in rotation direction, and calculated from the equivalent spring on the tip of PZT bender.
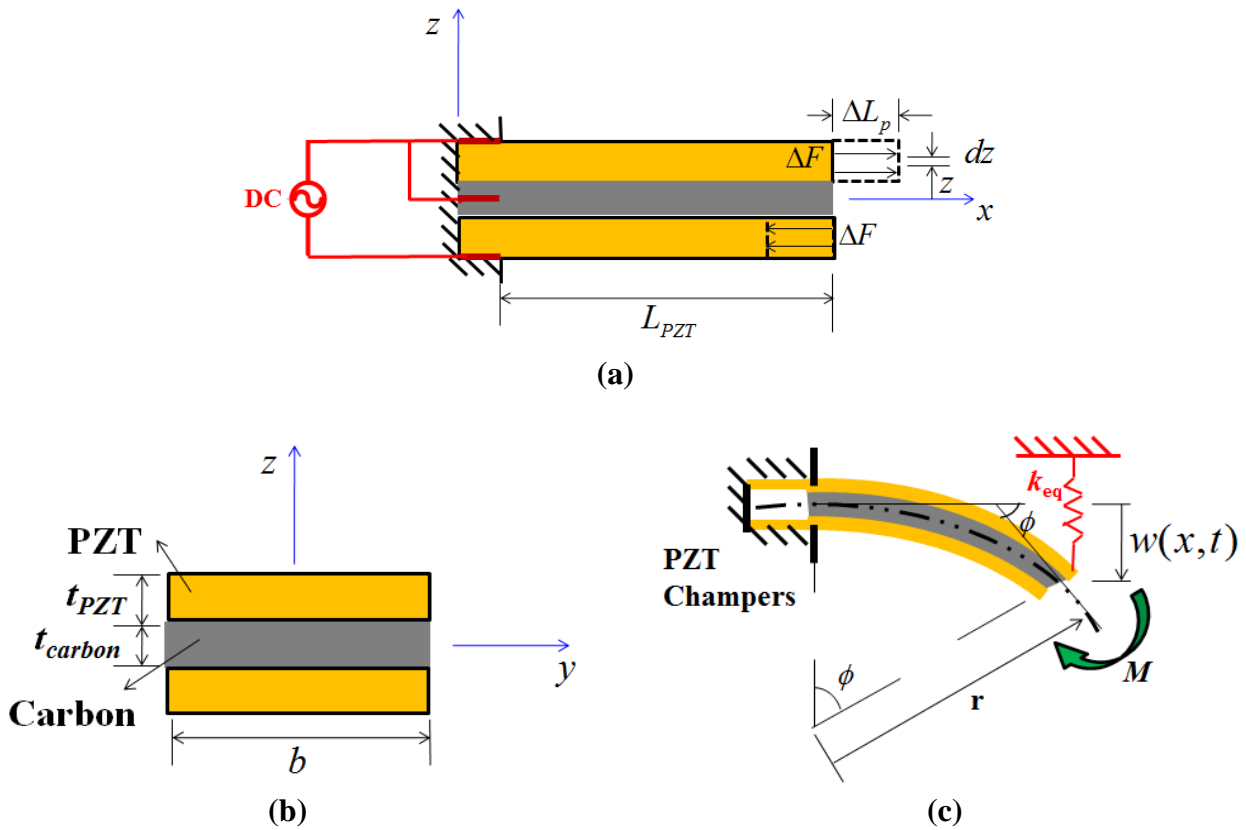
$$k_{PZT} = k_{eq} \frac{L_{PZT}}{2} \tag{5}$$

where k_{eq} in Figure 5(c) is presented as equivalent spring constant.

$$k_{eq} = \frac{2EI}{L_{PZT}^2} \tag{6}$$

Additionally, the rotary angle of PZT is:

$$\phi = \frac{M}{k_{PZT}} \tag{7}$$

Figure 5. Structure variables of triple-layer bimorph actuator: **(a)** crosswise view; **(b)** cross-section view; **(c)** deflection skew and equivalent spring.

3.2. Natural Frequency of PZT Bender

The motion of a cantilever beam can be represented as [16]:

$$c^2 \frac{\partial^4 w(x,t)}{\partial x^4} + \frac{\partial^2 w(x,t)}{\partial t^2} = 0, c = \sqrt{\frac{E_{eq} I_{eq}}{m'}} \tag{8}$$

By using the separation of variables method, the general solution can be expressed as

$$w(x,t) = X(x) \cdot T(t) \tag{9}$$

Replacing Equation (8) with Equation (9) yields

$$c^2 \frac{X''''(x)}{X(x)} = -\frac{T''(t)}{T(t)} = \omega_n^2 \tag{10}$$

The general solution of the mode shapes in *x*-direction can be expressed as

$$X_n(x) = A_1 \sin(\lambda_n x) + A_2 \cos(\lambda_n x) + A_3 \sinh(\lambda_n x) + A_4 \cosh(\lambda_n x), \; \lambda_n^4 = \frac{m'\omega_n^2}{E_{eq}I_{eq}} \tag{11}$$

The boundary condition of Equation (10) is:

$$\begin{cases} x = 0 \Rightarrow w = 0, \dfrac{\partial w}{\partial x} = 0 \\ x = L_{PZT} \Rightarrow EI\dfrac{\partial^2 w}{\partial x^2} = M = 0, \; EI\dfrac{\partial^3 w}{\partial x^3} = V = 0 \end{cases} \tag{12}$$

By substituting Equation (12) into Equation (11), the particular solution is

$$X_n(x) = \cosh\left(\frac{\lambda_n x}{L_{PZT}}\right) - \cos\left(\frac{\lambda_n x}{L_{PZT}}\right) - \alpha\left(\sinh\left(\frac{\lambda_n x}{L_{PZT}}\right) - \sin\left(\frac{\lambda_n x}{L_{PZT}}\right)\right) \tag{13}$$

where $\alpha = \dfrac{\sinh(\lambda_n L_{PZT}) - \sin(\lambda_n L_{PZT})}{\cosh(\lambda_n L_{PZT}) + \cos(\lambda_n L_{PZT})}$

The natural frequency is solved from the following equation:

$$\cos(\lambda_n x)\cosh(\lambda_n x) = -1; \; n = 1, 2, 3,... \tag{14}$$

For *n* = 1, the fundamental frequency of the bimorph PZT is:

$$\omega_1 = \sqrt{\frac{E_{eq}I_{eq}}{m'}} \cdot \frac{1.875^2}{2\pi L_{PZT}^2} \, (Hz) \tag{15}$$

where $m' = [\rho_{PZT}t_{PZT} + \rho_{carbon}t_{carbon}]b$.

3.3. Optimization

From the previous derivations of the equations, two objective functions of the optimization are selected: lateral displacement error $E(t_{PZT}, L_{PZT})$ and fundamental frequency $\omega(t_{PZT}, L_{PZT})$. Figure 6 shows the relationship between PZT arm actuator and disk, while Table 1 lists its symbols.

Figure 7 illustrates the optimization procedure, indicating that the PZT bender is optimized. Of the two coupling optimization processes, optimization 1 determines objective functions and sets the initial search interval and accuracy. Meanwhile, optimization 2 copes with constraint conditions for the process. The optimization of length L_{PZT} and thickness t_{PZT}, which minimize objective functions to PZT, are 14.13 mm and 0.11 mm after 64 and 59 iterations, respectively.

Figure 8 plots two parameters, rotary angle ϕ [Equation (7)] and fundamental frequency ω_1 [Equation (15)] as a function of effective length. The crossover point is selected to verify the optimization results. Figure 9 illustrates the hysteresis curve of PZT displacement with maximum point is 4 mm when input a sine wave signal is swept from −125 to 125 V. Finally, the experimental

results in Figure 10 demonstrate two modes frequency at 985 Hz and 5.8 kHz. Table 2 summarizes the modal analysis results between the numerical optimization and experiments, in which the errors vary by about 1.86% and 3.14%, respectively.

Figure 6. Geometry and coordinates for the dual stage actuator based on electromagnetism and mechanism (*t* and *r* present tangential and radius direction respected to the disk).
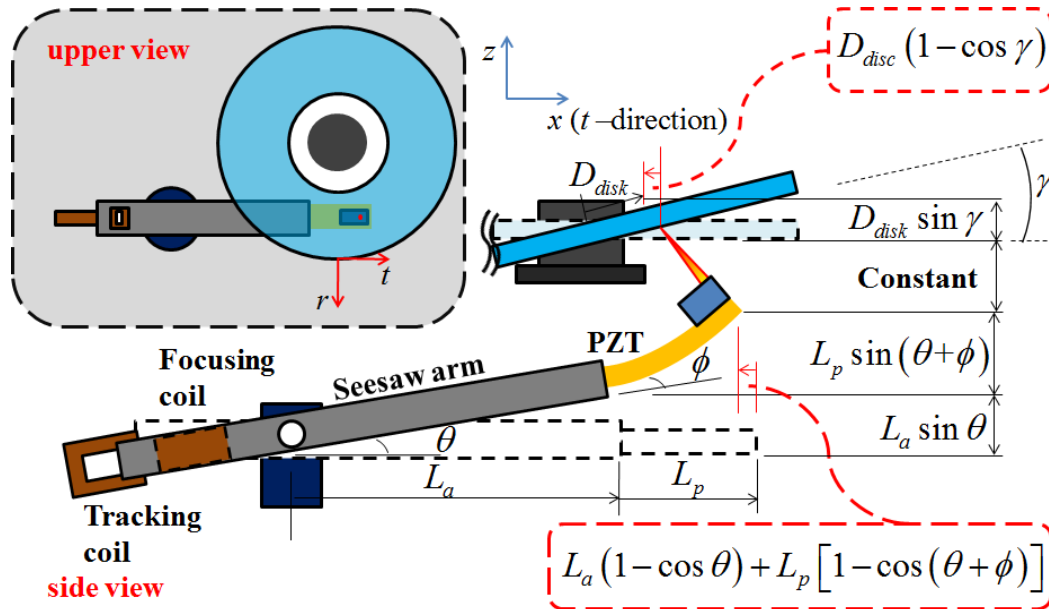

Table 1. Parametric optimization investigates the design parameters.

	Optimization 1	Optimization 2
Objective function	$E = L_{arm}(1-\cos\theta) + L_{PZT}(1-\cos(\theta+\phi))$ $-D_{disk}(1-\cos\gamma)$	$\omega_1 = \sqrt{E_{eq}I_{eq}/m'} \times \dfrac{1.875^2}{2\pi L_{PZT}^2}$
Optimization parameter	L_{PZT}	t_{PZT}
upper/lower bound	$10 \leq L_{arm} \leq 17$ $10 \leq L_{PZT} \leq 17$	$10 \leq L_{PZT} \leq 17$ $0.1 \leq t_{PZT} \leq 1.0$
Constrain	$L_{arm} + L_{PZT} = 27(mm)$ $\theta + \phi - \gamma = 0(rad)$	$2t_{PZT} + t_{carbon} \leq 3(mm)$
Algorithm	*Medium-scale: SQP, Quasi-Newton, line-search*	
Iterations	64	59
Optimization value	**0.271**	**985 Hz**
FuncCount	485	603
Stepsize	0.3014	0.31
Firstorderopt	80.1485	79.3485
Constrviolation	15.0831	21.2495
result	**14.13**	**0.11**

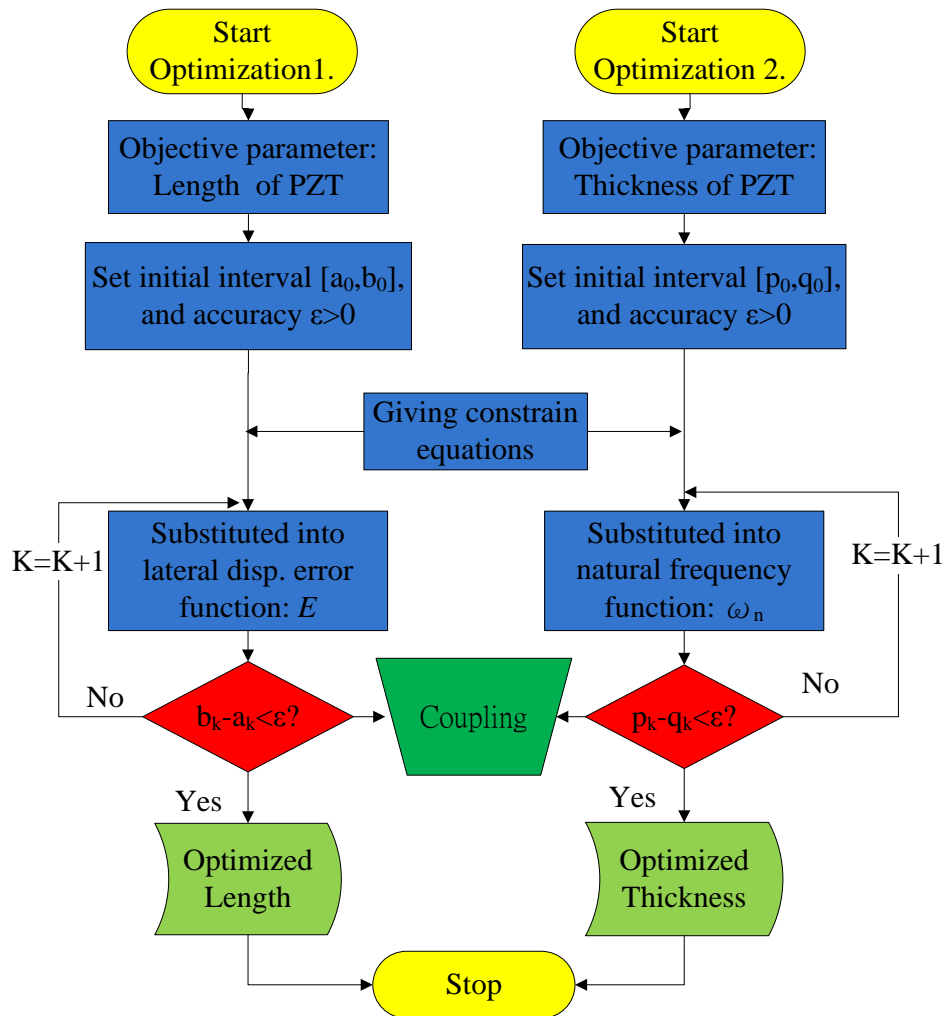**Figure 7.** Flowchart of the PZT optimization procedure.

Figure 8. Effective length *versus* optimal balance between rotary angle (rad) and natural frequency (Hz).
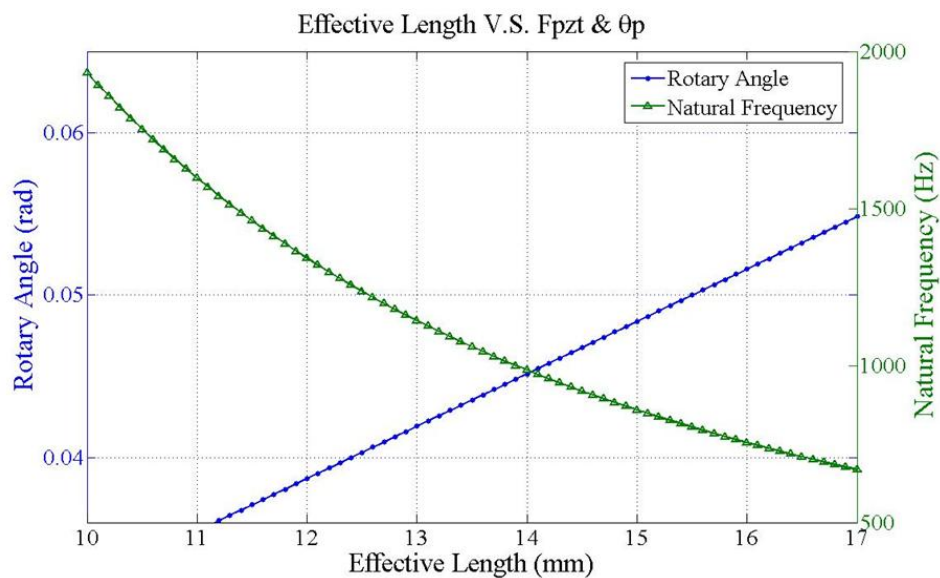
Figure 9. Deflection curve of hysteresis loop in a bimorph bender with the applied voltage swing from ±125 V.
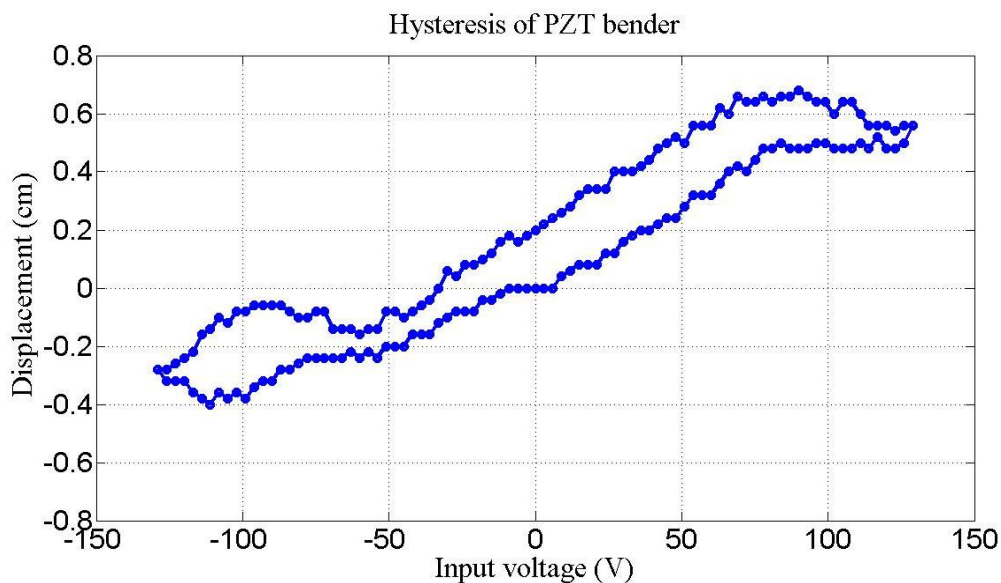

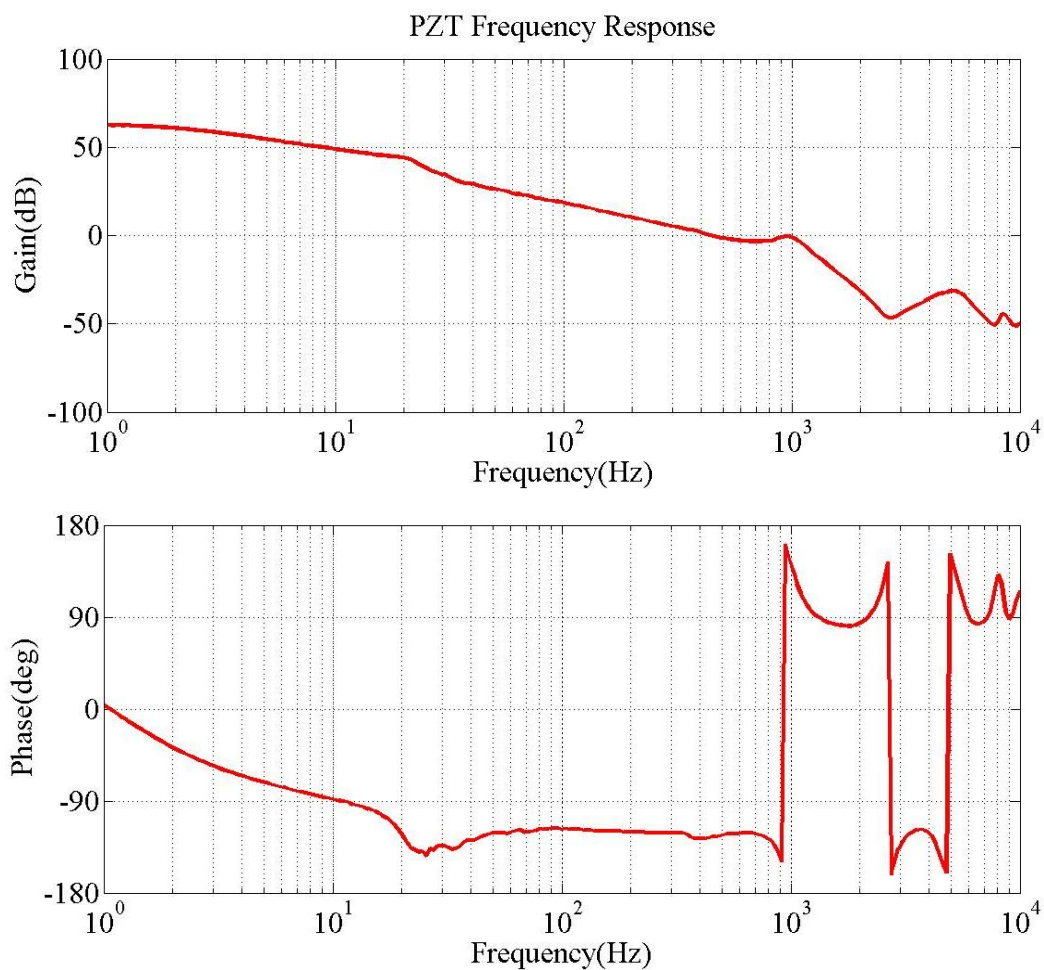**Figure 10.** Measured frequency response of optimum PZT bender.

Table 2. Verification of numerical optimization.

Resonant Frequency(<10 kHz)	Numerical calculation	Experimental result	Error
1st mode	967	985	1.86%
2nd mode	6,065	5,874	3.14%

3.4. Absorber Mass Tuning

Several attempts have been made to seek optimum absorber parameters when the main system has significant damping. Den Hartog first tackled the optimum solution of a tuned mass damper that is connected to a primary system with the intention of reducing its dynamic response [20]. An optimal broadband attenuation was then achieved by a dynamic absorber design proposed by Ormondroyd and Den Hartog [21]. Based on their fixed-point theory, Brock found the optimum tuning parameter and defined the optimality for the optimum absorber damping [22]. By adopting a frequency locus approach, Thompson found the optimal damper parameters that minimize the structural response [23].

The equation of the damped model in Figure 11 can be expressed as

$$\begin{cases} m_{sys}\ddot{x}_1 - c_{abs}\left(\dot{x}_2 - \dot{x}_1\right) - k_{abs}\left(x_2 - x_1\right) + c_{sys}\dot{x}_1 + k_{sys}x_1 = f_0 \\ m_{abs}\ddot{x}_2 + c_{abs}\left(\dot{x}_2 - \dot{x}_1\right) + k_{abs}\left(x_2 - x_1\right) = 0 \end{cases} \tag{16}$$

where m_{sys}, c_{sys} and k_{sys} denote the mass, damping and stiffness coefficient of primary actuator system; m_{abs}, c_{abs}, and k_{abs} refer to the mass, damping, and stiffness coefficient of tunable vibration absorber system; f_0 and ω denote the amplitude and frequency of the exciting force, respectively; and x_1 and x_2 represent the displacement of the actuator and the absorber, respectively. The normalized amplitude of the steady-state response of the primary mass can be expressed as:

$$\begin{cases} x_1 = X_1 e^{j\omega t} \\ x_2 = X_2 e^{j\omega t} \\ f_0 = F_o e^{j\omega t} \end{cases} \tag{17}$$

Figure 11. A suspended mass m_{sys} interfered with a driven force f_0. The absorber mass m_{abs} is maneuvered by the reaction force to reduce displacement x_1.
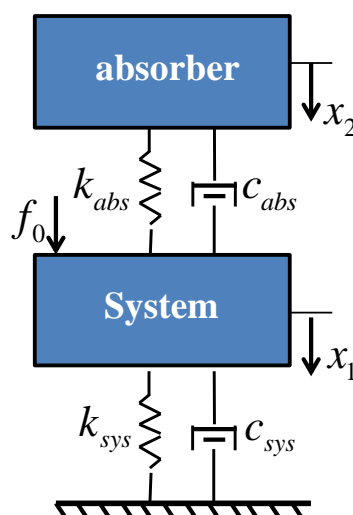
The amplitudes of the system displacement, X_1, are expressed as:

$$X_1 = \frac{\left(k_{abs} - m_{abs}\omega^2\right) + j\omega c_{abs}}{\left\{\begin{array}{l}\left(k_{sys} - m_{sys}\omega^2\right)\left(k_{abs} - m_{abs}\omega^2\right) - \left(k_{abs}m_{abs} + c_{sys}c_{abs}\right)\omega^2 \\ + j\omega\left[c_{abs}\left(k_{sys} - m_{sys}\omega^2 - m_{abs}\omega^2\right) + c_{sys}\left(k_{abs} - m_{abs}\omega^2\right)\right]\end{array}\right\}} \cdot F_0 \tag{18}$$

Taking the absolute of X_1:

$$|X_1| = F_0 \sqrt{\frac{\left[\left(\frac{k_a}{m_a} - \omega^2\right)^2 + \left(\frac{C_a}{m_a}\omega\right)^2\right]\left(\frac{k_{sys}}{m_{sys}}\right)^2}{\left[\left(\frac{k_{sys}}{m_{sys}} - \omega^2\right)\left(\frac{k_a}{m_a} - \omega^2\right) - \left(\frac{k_a}{m_a}\frac{m_a}{m_{sys}} + \frac{C_a}{m_a}\frac{C_{sys}}{m_{sys}}\right)\omega^2\right]^2 + \left[\frac{C_a}{m_a}\left(\frac{k_{sys}}{m_{sys}} - \omega^2 - \frac{m_a}{m_{sys}}\omega^2\right) + \frac{C_{sys}}{m_{sys}}\left(\frac{k_a}{m_a} - \omega^2\right)\right]^2}} \tag{19}$$

Substituting the natural frequency, $\omega_{abs} = \sqrt{\frac{k_{abs}}{m_{abs}}}$ and $\omega_{sys} = \sqrt{\frac{k_{sys}}{m_{sys}}}$, into the Equation (19), the normalized transfer function of an actuator is

$$G = \frac{|X_1 \cdot k_{sys}|}{|f_0|} = |X_1| \cdot \frac{k_{sys}}{F_0} = \sqrt{\frac{A^2(\alpha,\beta) + 4B^2(\zeta_{abs},\alpha,\beta)}{C^2(\mu,\zeta_{sys},\zeta_{abs},\alpha,\beta) + 4D^2(\mu,\zeta_{sys},\zeta_{abs},\alpha,\beta)}} \tag{20}$$

where:

$$A(\alpha,\beta) = 1 - \frac{\alpha^2}{\beta^2} \;,\;\; B(\zeta_{abs},\alpha,\beta) = \zeta_{abs}\frac{\alpha}{\beta}$$

$$C(\mu,\zeta_{sys},\zeta_{abs},\alpha,\beta) = \frac{\alpha^4}{\beta^2} - \left(\frac{4\zeta_{sys}\zeta_{abs}}{\beta} + \frac{1}{\beta^2} + \mu + 1\right)\alpha^2 + 1$$

$$D(\mu,\zeta_{sys},\zeta_{abs},\alpha,\beta) = \zeta_{abs}\left(\frac{\alpha}{\beta} - \frac{\alpha^3}{\beta} - \mu\frac{\alpha^3}{\beta}\right)\alpha^2 + \zeta_{sys}\left(\alpha - \frac{\alpha^3}{\beta^2}\right)$$

and the parameters are:

$$\mu = \frac{m_{abs}}{m_{sys}} \,,\, \alpha = \frac{\omega}{\omega_{sys}} \,,\, \xi_{sys} = \frac{C_{sys}}{2\sqrt{m_{sys}k_{sys}}} \,,\, \beta = \frac{\omega_{abs}}{\omega_{sys}} \,,\, \xi_{abs} = \frac{C_{abs}}{2\sqrt{m_{abs}k_{abs}}}$$

According to Den Hartog's theorem [17], the ratio of natural frequency between absorber and system is:
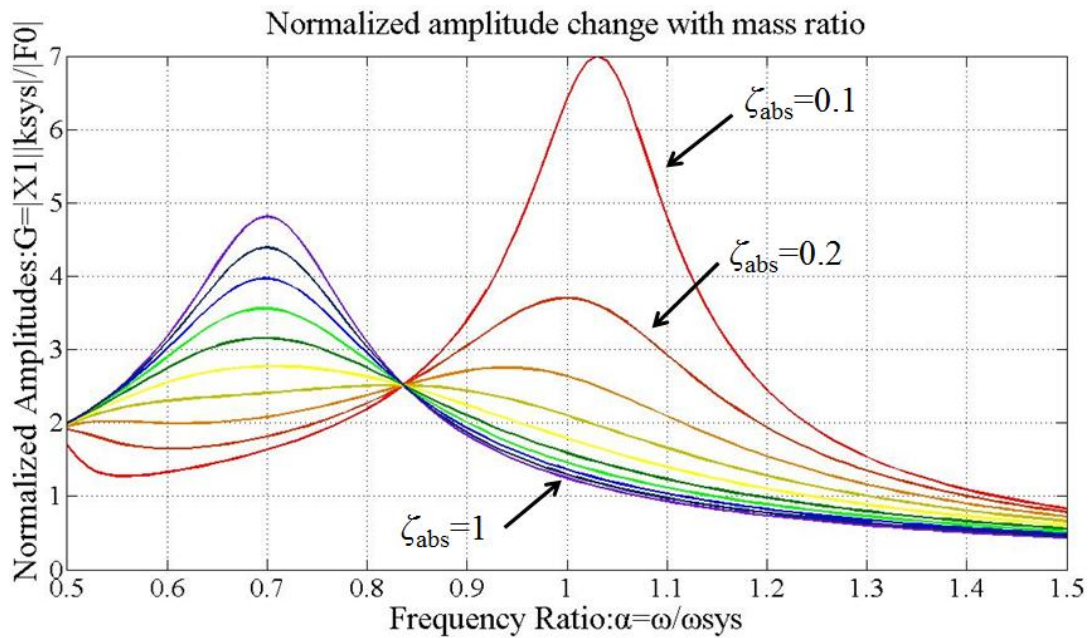
$$\beta^* = \frac{1}{1+\mu} \tag{21}$$

Figure 12(a) displays the relationship between μ and G. Hence, the peak is reduced with enlarged μ. According to Figure 12(b), the resonance peak frequency increases when ζ_{abs} decreases from 1 down to 0.1. The optimal damping ratio of the absorber, $\zeta_{abs}{}^*$, is estimated as:

$$\zeta_{abs} = \zeta_{abs}{}^* = \sqrt{\frac{3\mu}{8(1+\mu)}} \tag{22}$$

Figure 12. Normalized amplitudes of vibrations: **(a)** $\zeta_{abs} = 1$ (fixed), $\mu = 0.1\sim1$. **(b)** $\mu = 1$ (fixed), $\zeta_{abs} = 0.1\sim1$.
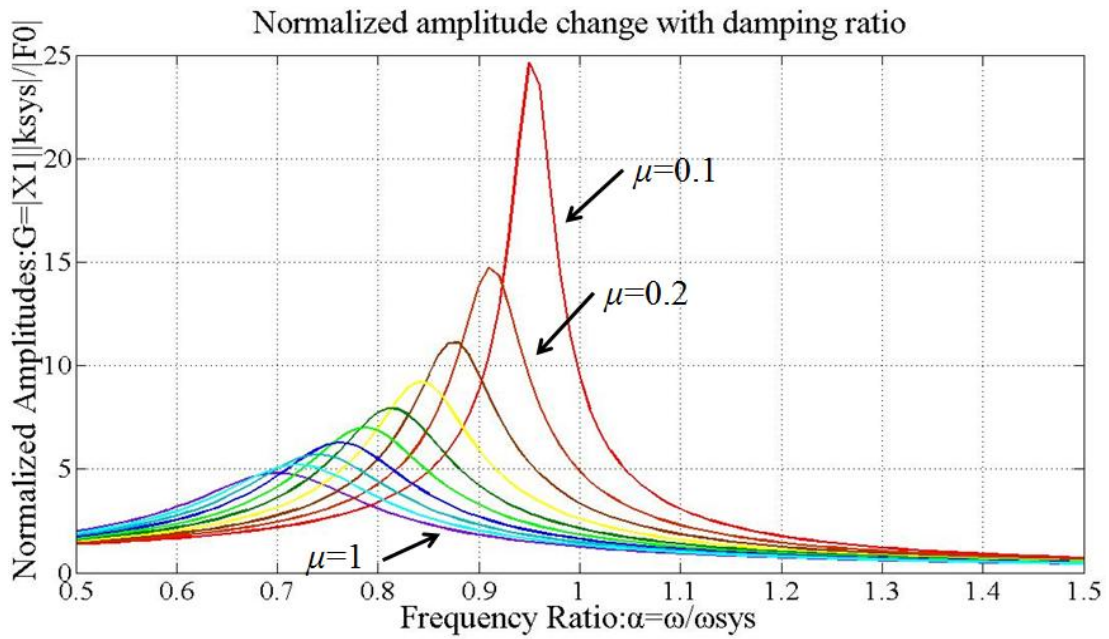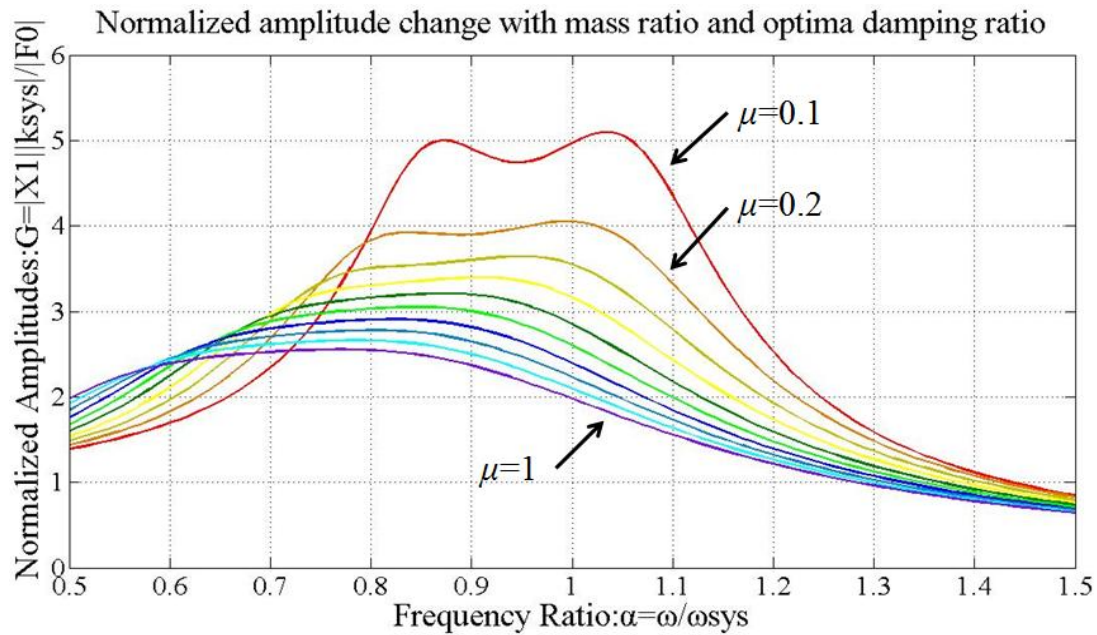

(a)

(b)

Figure 13 shows the normalized amplitude G as a function of μ. By assigning the optimal damping ratio ζ_{abs} and mass ratio μ, the vibration magnitudes are decreased effectively. (Therefore, the actual values of mass and stiffness of TVA are determined by selecting $\mu = 0.8$ and $\zeta_{abs}^{*} = 0.408$.

Figure 13. Normalized amplitudes of vibrations when $\mu = 0.1 \sim 1$ and $\zeta_{abs} = \zeta_{abs}{}^{*}$.

4. Experiments

4.1. Evaluation of Dynamic Performance

Figure 14 shows a prototype of proposed dual-stage PZT-VCM actuator assembly with small passive TVA actuation. The dynamic response of the dual-stage actuator and the PZT bender is obtained experimentally by LDV and a frequency response analyzer, as shown in Figure 15.

Figure 16 shows the effectiveness of TVA vibration suppression. The performance and robustness of the absorber are further enhanced by using optimal processes for dual stage actuation. According to simulation and experimental results, the passive TVA reduces the system vibration by 80% with respect to the peak amplitudes.

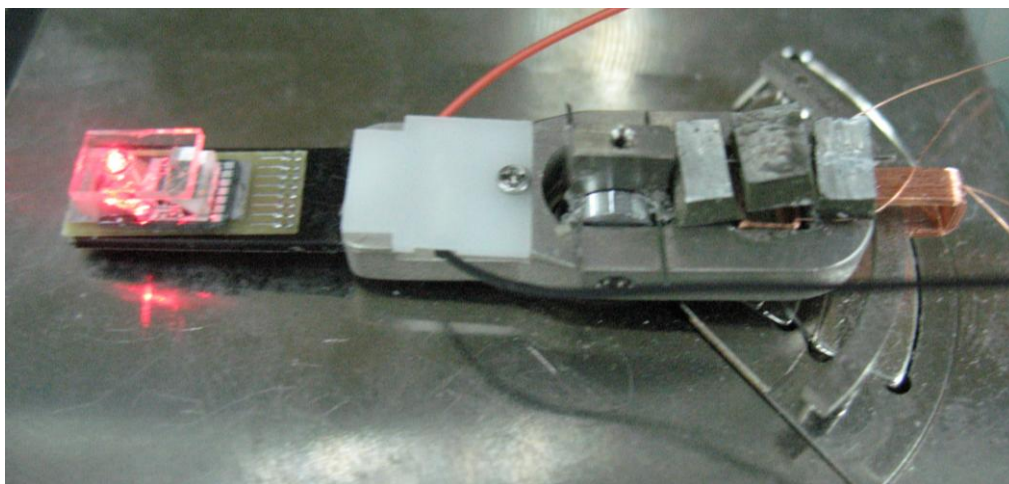**Figure 14.** Prototype of the dual-stage seesaw actuator.

Figure 15. Experimental setup of the dual stage actuator utilized in the active vibration control scheme and measurement point of the laser vibrometer.
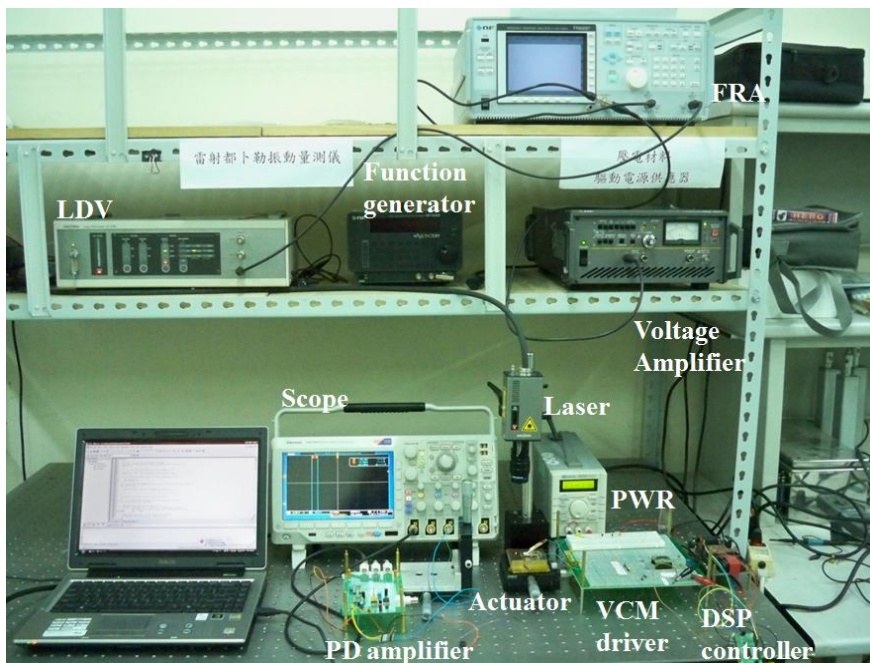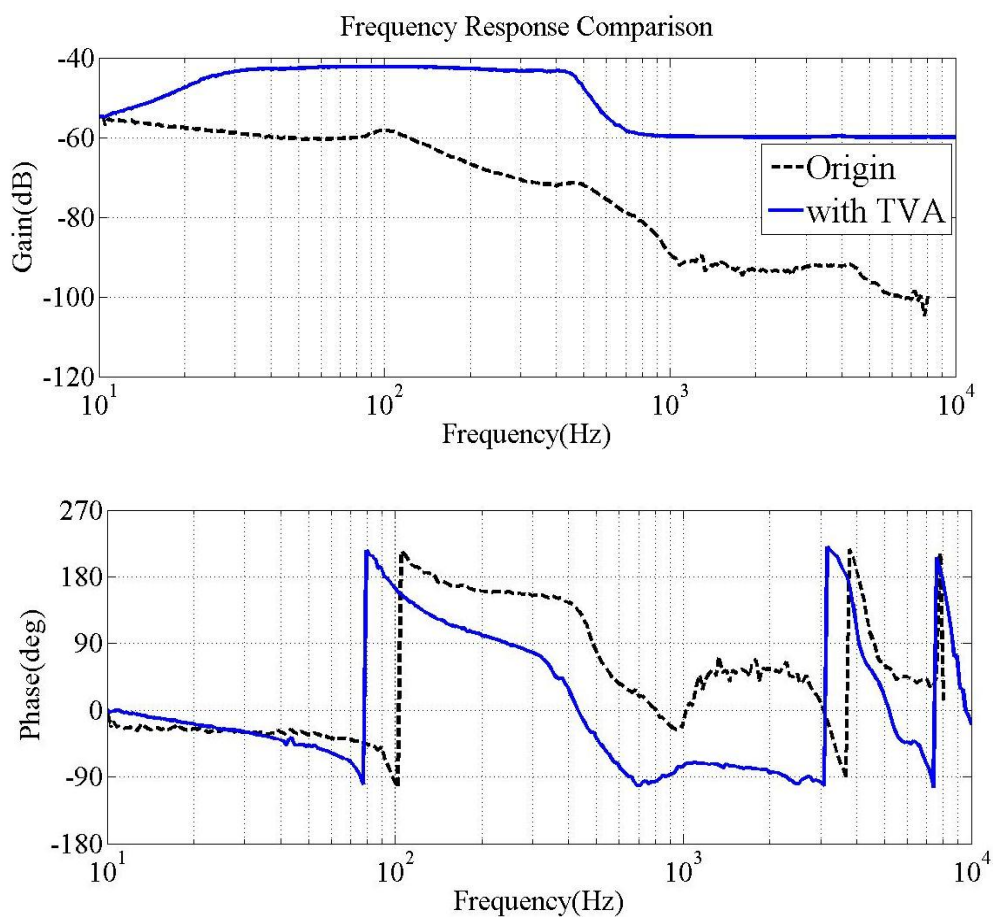

Figure 16. Frequency responses of actuator assemblies with (solid line) and without (dashed line) TVA unit.

Design of the PZT loop compensator in the dual-stage actuator expands the bandwidth of the overall system. The primary VCM continuously provides coarse positioning, while the secondary actuator gives fine positioning, vibration and disturbances rejection. Figure 17 illustrates the open loop frequency response of the VCM and PZT dual-stage actuator, compared with the original single-stage VCM actuator.

Figure 17. Single- and dual-stage actuated suspension frequency response: VCM input to head displacement (dash line); VCM and PZT combined actuation input to head displacement (solid line).
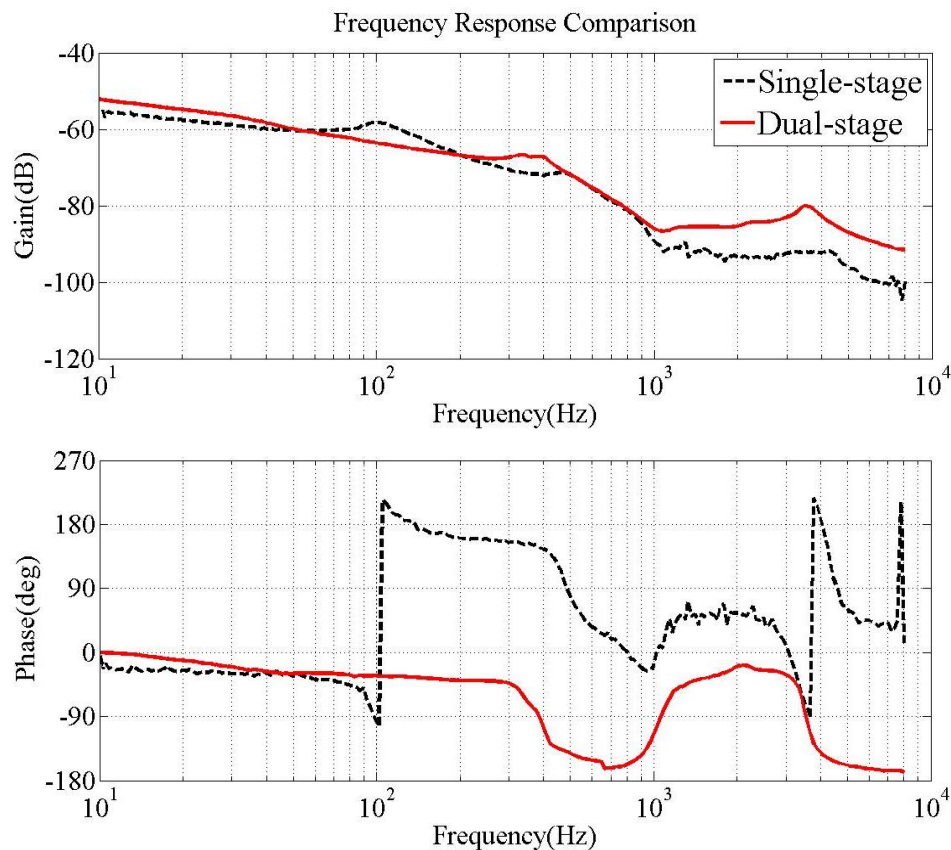
The open loop bandwidth of the dual-stage system is approximately 3.8 kHz, with a phase margin of 30 degrees and a gain margin of 5 dB. This represents a significant enhancement over the single-stage VCM system, which has a 0.46 kHz bandwidth for the same stability margins. The PZT actuator can reject high frequency disturbances. Notably, the resonant peak of the PZT actuator at 0.9 kHz is lower than the open loop bandwidth and does not pose stability problems.

4.2. Tilt Angle Compensation

Figure 18(a) illustrates the simulated focusing error signal (S-curve) generated by the actuator tilting from -0.5° to 0.5°, whereas the measured asymmetric S-curve is shown in Figure 18(b) for comparison. The astigmatic returning laser spot deteriorates considerably due to the tilt actuation, causing the asymmetric peak shapes of the S-curve. This unbalanced S-curve signal reduces the accuracy of optical sensing. The optical compensation for dual stage actuator is evaluated by designing

the schematic layout of the reflection geometry for tilt measurement [24-26], as shown in Figure 19. The rotary angle measurement is performed by mounting a target 45 ° micro-prism on the precision VCM-Driven micro-positioning stage. The 635 nm wavelength laser, which is used to adjust tracking angle of dual-stage actuator, produces horizontal beam (green line) and passes through the collimating lens, the polarized beam splitter (PBS), the quarter-wave plate (QWP) to form circular polarization beam and focusing on the side of actuator by objective lens. The returning beam is reflected by the PBS and projected on the collimating detector. Furthermore, the LDV laser beam (red line, vertical) is focusing on the photo-diode to measure the dynamic tilt error motions of focus operation by varying the driving frequency in the range of 5–200 Hz. The distance of the seesaw actuator over the focus actuation stroke is 400 μm or less.

Figure 18. Intensity profiles of the reflected beam on the photo-diode and the output astigmatism signals (S-curve), **(a)** simulation; **(b)** measurement.
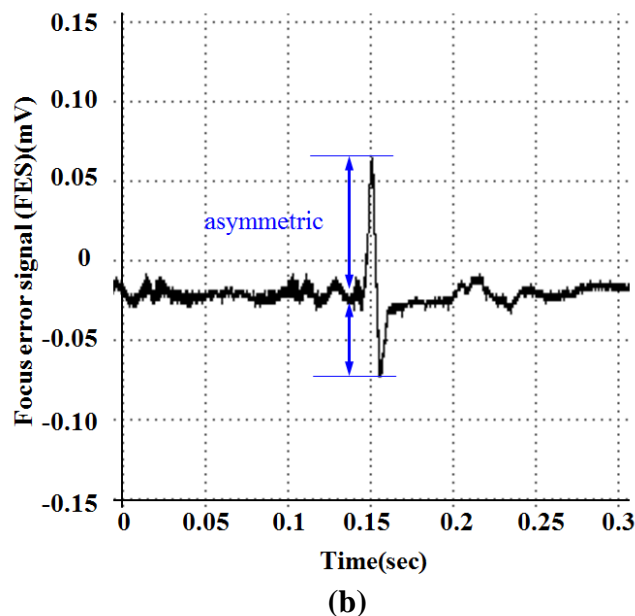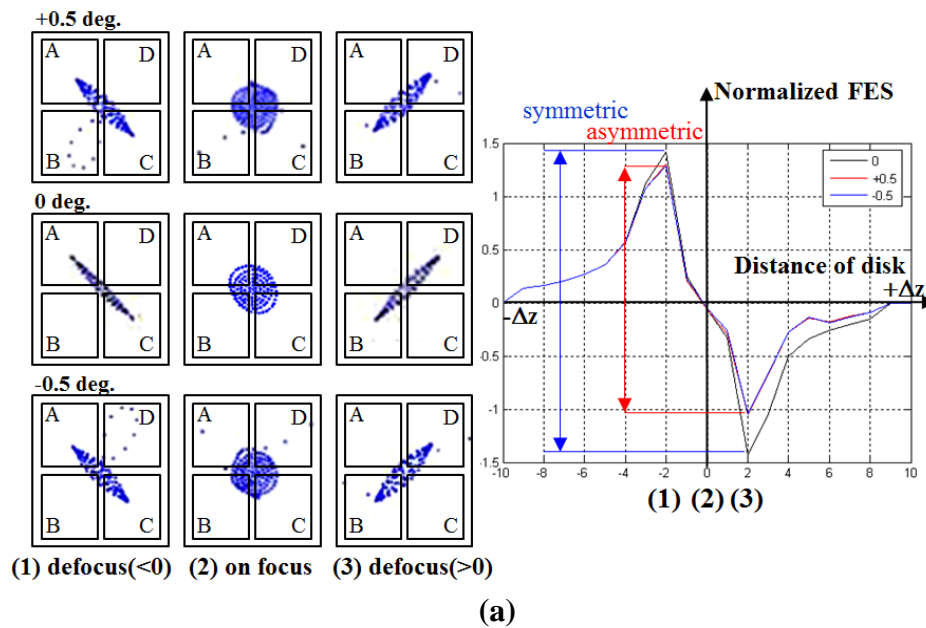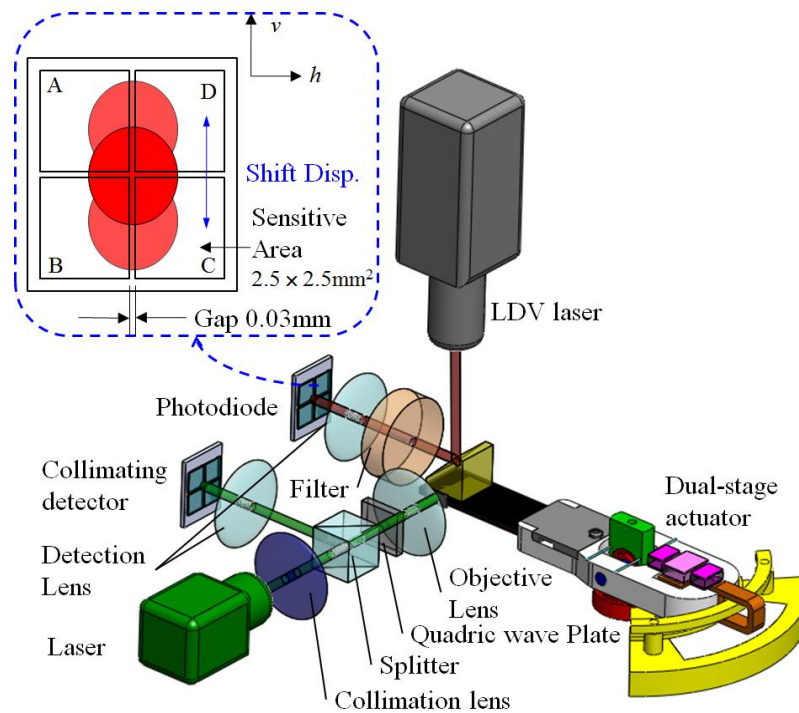

(a)

(b)

Figure 19. Geometrical model to detect the optical angle: optical layout for the differential detection method and focal spot shifts along the photodiode (*v*-direction).

The proposed astigmatic detection method combined with differential phase detection (DPD) is verified through simulation and experimental results. By using the quadrant photo detector array, the astigmatic signal is generated (based on the phase difference between the sum of the diagonal elements, as shown in Equation (22).

Focus error signal (FES), *f*:

$$f = \frac{(A+C)-(B+D)}{(A+B+C+D)} \times 100\% \qquad (23)$$

The DPD signal is defined *versus* the misalignment of the photo-detector in the plane (v, h) by using the following calculation [27,28].

DPD signal, d_h:

$$d_h = \frac{(A+B)-(C+D)}{(A+B+C+D)} \times 100\% \qquad (24)$$

DPD signal, d_v:

$$d_v = \frac{(A+D)-(B+C)}{(A+B+C+D)} \times 100\% \qquad (25)$$

where d_h and d_v represent the misalignments along the horizontal (*h*) and vertical (*v*) the direction, respectively.

Feasibility of the proposed secondary stage PZT-actuator to compensate for the tilt actuation induced by the primary VCM actuator is demonstrated by conducting an experiment in which the dual stage actuator is kept in the in-focus condition. Figure 20 summarizes the experimental results by

moving the prism with reflection geometry. The vertical (black) and horizontal (red) tilt angle are obtained based on differential phase variation with 5 Hz sine-wave excitation. Although the vertical angular displacement involves roll as well as pitch rotation, the phase variation from roll vibration is sufficiently small to be negligible compared with the actuator nutation.

Figure 20. Comparison of two actuation directions with the DPD measurement results from the tilt error signal (black) and lateral deviation (red).
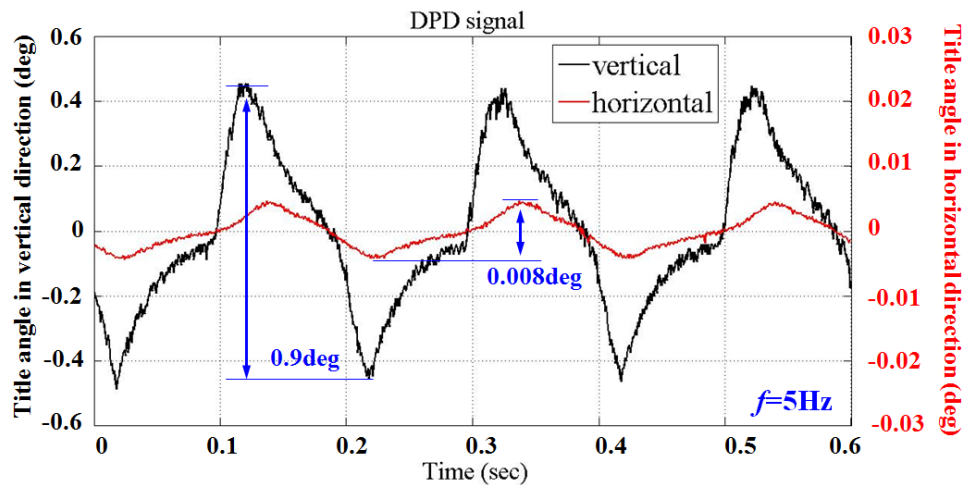
Both results closely correspond to the numerical calculations. The measurement accuracy of the photo-detector is validated. Figure 21 shows the tilt motions for both single and dual stage control. A sinusoidal signal with a frequency of 5 Hz and voltage amplitude of 6 V is applied to the seesaw actuator. As mentioned earlier, the angular displacement is within the restricted range ±0.19 ° (peak to peak) for the dual stage actuation than ±0.45 ° (peak to peak) for single-stage control. The tilt signal variance from a single-stage drive is reduced by 60% with the implementation of this dual stage compensation. Measurement results demonstrate a high stability for the application of adjusting the inclination angle of the optical axis with precision positioning, capable of satisfying the requirement for small tilt angle compensation of a dual stage actuator.

Figure 21. Experimental verification of dual stage compensation: with (red line) and without (black line) piezo-actuated stage actuator.
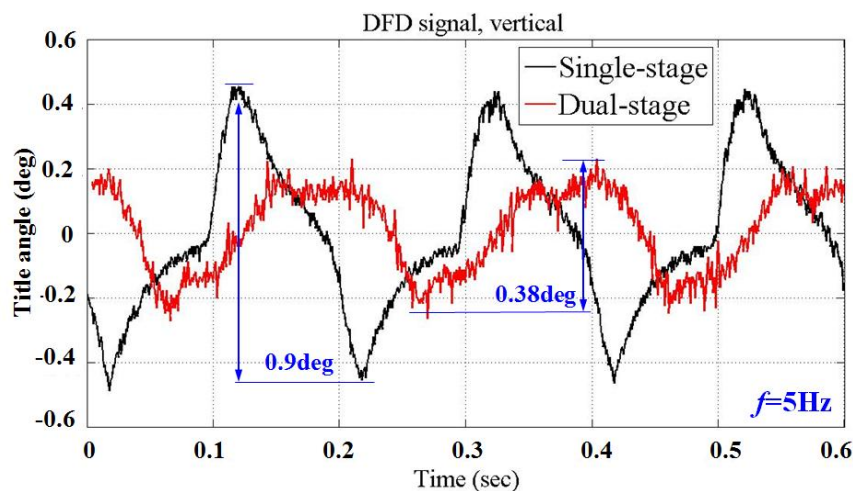
5. Conclusions

This work presents a miniaturized seesaw swivel actuator and suspension assembly with a piezoelectric-based micro-actuator and TVA absorber. Among the unique features of the proposed dual stage actuator include a rotary actuator for track-following and a combined piezo-VCM actuated suspension nutation for laser focusing. By using the optimization procedure, the original design is improved in terms of bandwidth and stability. The dynamic response of the dual-stage actuator is also shown, in which the PZT actuator rejects a higher frequency disturbance. The difference between the experimental frequency response of PZT bender and the numerical results is within 5.6%. Lower than the open loop bandwidth, the resonant peak of the PZT-actuator at 0.9 kHz does not pose stability problems. Simulation and experimental results indicate that the passive TVA reduces the system vibration by 80% with respect to the peak amplitudes. This work also investigates the relationship between the tilt sensor sensitivity and working distance of the dual stage actuator based on laser auto-collimation. The tilt variance of optical axis is reduced by 60% from a single-stage drive with the implementation of PZT compensation. Performance optimization of the combined piezo-VCM actuator is also evaluated to demonstrate the effectiveness of the proposed optical sensing applications.

References

1. Shih, H.F.; Chang, C.L.; Lee, K.J.; Chang, C.S. Design of optical head with holographic optical element for small form factor drive systems. *IEEE Trans. Mag.* **2006**, *41*, 1058-1060.
2. Shih, H.F.; Lee, Y.C.; Chiu, Y.; Chao, D.W.C.; Lin, G.D.; Lu, C.S.; Chiou, J.C. Micro Objective Lens with NA 0.65 for The Blue-light Small-form-factor Optical Pickup Head. *Optics Express* **2008**, *16*, 13150-13157.
3. Chou, P.C.; Lin, Y.C.; Cheng, S. Optimization of Seesaw Swing Arm Actuator Design for Small Form Factor Optical Disk Drive. *Jpn. J. Appl. Phys.* **2010**, *49*, 052502.
4. Chou, P.C.; Lin, Y.C.; Cheng, C. A Novel Seesaw Swivel Actuator Design and Fabrication. *IEEE Trans. Mag.* **2010**, *46*, 2603-2610.
5. Yeak-Scranton, C.E. Novel Piezoelectric Transducers to Monitor Head-disk Integrations. *IEEE Trans. Mag.* **1986**, *22*, 1011-1016.
6. Tagawa, N. State of The Art for Nanospacing Flying Head Slider Mechanisms in Magnetic Recording Disk Storage .*Wear* **1993**, *168*, 43-47.
7. Kajitani, H.; Hashimoto, M.; Tagawa, N. Dynamic Loading Criteria for 3-1/2 Inch Inline HDD Using Multilayer Piezoelectric Load/Unload Mechanism. *IEEE Trans. Mag.* **1991**, *27*, 5079-5081.
8. Tominaga, J.; Watabe, T.; Yoshimoto, S. A Circular Arc Slider with a High Flying Height Supported by Parallel Flat Springs for Optical Disc Devices. *Microsyst. Technol.* **2007**, *13*, 1131-1139.
9. Chang, C.S.; Liu, T.S.; Tang, Y.C. A Tracking Motion Approach For a Piezotube Actuator in a Disk Drive subject to Disk Deformation and Disturbance. *Smart Mater. Struct.* **2007**, *16*, 1542-1548.

10. Yang, W.; Lee, S.Y.; You, B.J. A Piezoelectric Actuator with A Motion-Decoupling Amplifier for Optical Disk Drives. *Smart Mater. Struct.* **2010**, *19*, 065027.

11. Chung, J. Vibration Absorber for Reduction of the In-Plane Vibration in an Optical Disk Drive. *IEEE Trans. Consum. Electron.* **2004**, *50*, 552-557.

12. Heo, J.W.; Chung, J. Vibration and Noise Reduction of an Optical Disk Drive by Using a Vibration Absorber. *IEEE Trans. Consum. Electron.* **2002**, *48*, 874-878.

13. Chang, C.S.; Liu, T.S. Design of Adaptive Dynamic Absorber to Reduce Optical Disk Drive Vibration at Multiple Rotating Speeds. *Jpn. J. Appl. Phys.* **2006**, *45*, 1120-1123.

14. Jiang, L.; Miles, R.N. A Passive Damper for the Vibration Modes of the Head Actuator in Hard Disk Drives. *J. Sound Vibra.* **1999**, *220*, 683-694.

15. Kuwajima, H.; Kita, H.; Hashi, H.; Miyamoto, M.; Ueno, Y.; Inagaki, T.; Matsuoka, K. Development of Balanced-type High Shock Suspension for 0.85-in Hard Disk Drive. *IEEE Trans. Mag.* **2006**, *42*, 255-260.

16. DeVoe, D.L.; Pisano, A.P. Modeling and Optimal Design of Piezoelectric Cantilever Microactuators. *IEEE J. Microelectromech. Syst.* **1997**, *6*, 266-270.

17. Weinberg, M.S. Working Equations for Piezoelectric Actuators and Sensors. *IEEE J. Microelectromech. Syst.* **1999**, *8*, 529-533.

18. Krommer, M. On the Correction of the Bernoulli–Euler Beam Theory for Smart Piezoelectric Beams. *Smart Mater. Struct.* **2001**, *10*, 668-680.

19. Ha, S.K.; Kim, Y.H. Analysis of a Piezoelectric Multimorph in Extensional and Flexural Motions. *J. Sound Vibra.* **2002**, *253*, 1001-1014.

20. Den Hartog, J.P. *Mechanical Vibrations*; McGraw-Hill, Inc.: New York, NY, USA, 1956.

21. Ormondroyd, J.; Den Hartog, J.P. Theory of The Dynamic Vibration Absorber Transactions of the *Am. Soc. Mech. Eng.* **1928**, *50*, 9-22.

22. Brock, J.E. A Note on the Damped Vibration Absorber. *J. Appl. Mech.* **1946**, *68*, A-284.

23. Thompson, A.G. Optimizing the Untuned Viscous Dynamic Vibration Absorber with Primary System Damping. *J. Sound Vibra.* **1980**, *73*, 469-412.

24. Kim, S.H.; Kim, J.H.; Lee, Y.H.; Yang, H.; Park, J.Y.; Park, K.S.; Park, Y.P. Tilt Error Measurement and Compensation Method for the Holographic Data Storage System Using Disturbance Observer. *IEEE Trans. Mag.* **2009**, *45*, 2248-2251.

25. Doh, T.Y.; Ma, B.I.; Choi, B.H.; Park, I.S.; Chung, C.S.; Lee, Y.H.; Kim, S.J.; Shin, D.H. Radial Tilt Detection Using one Beam and its Compensation in A High-density Read Only Memory. *Jpn. J. Appl. Phys.* **2001**, *40*, 1680-1683.

26. Lin, D.; Yue, Z.; Song, N.; Meng, Y.; Yin, C. A Double Common-path Heterodyne Interferometer for The Measurement of Flying Height Modulation. *Meas. Sci. Technol.* **2008**, *19*, 055303.

27. Shinoda, M.; Nakai, K.; Mori, K. Dependence of Differential Phase Detection Signals on Astigmatism in A Focused Spot. *Jpn. J. Appl. Phys.* **2004**, *43*, 4870-4875.

28. Saito, Y.; Arai, Y.; Gao, W. Investigation of An Optical Sensor for Small Tilt Angle Detection of A Precision Linear Stage. *Meas. Sci. Technol.* **2010**, *21*, 054006.